npj | climate and atmospheric science

Article

Published in partnership with CECCR at King Abdulaziz University

https://doi.org/10.1038/s41612-024-00608-2

Evolving winter atmospheric teleconnection patterns and their potential triggers across western North America

Jueun Lee [1], S.-Y. Simon Wang[2], Seok-Woo Son [3], Daehyun Kim [3], Jee-Hoon Jeong[4], Hyungjun Kim [5] & Jin-Ho Yoon [1]

We present a comprehensive analysis diagnosing the primary factors driving the observed changes in major atmospheric teleconnection patterns in the Northern Hemisphere winter, including the Pacific North American pattern (PNA), North Atlantic Oscillation (NAO), and North American winter dipole (NAWD), with particular focus on their roles in shaping anomalous weather across North America. Our investigation reveals a consistent influence of the NAWD over seven decades, contrasting with fluctuating impacts from PNA and minor impacts from NAO. In particular, an emergent negative correlation between the NAWD and PNA, signaling a shifted phase of teleconnection patterns, is identified. Such a relationship change is traced to enhanced upper-level ridges across western North America, reflecting a reinforced winter stationary wave. Through attribution analysis, we identify greenhouse gas emissions as a probable driver for the northward drift of the Asia-Pacific jet core, which, aided by orographic lifting over the Alaskan Range, subsequently amplifies the winter stationary wave across western North America. This work emphasizes the pronounced effect of human-induced global warming on the structure and teleconnection of large-scale atmospheric circulation in the Northern Hemisphere winter, providing vital perspectives on the dynamics of current climate trends.

Western North America has experienced more extreme climate events in recent years, leading to billions of dollars in damages. For example, from 2011 to 2015, a persistent upper-level ridge in the winter mean caused prolonged and unprecedented droughts in California and neighboring states[1–4]. In 2017, the atmospheric circulation pattern flipped into an anchoring trough in western North America, resulting in extreme precipitation and floods over California[4]. These weather patterns are consistently linked to the North American Winter Dipole (NAWD), a 'Ridge-Trough' feature that coincides with the winter stationary wave over North America[5].

Historically, the Pacific North American pattern (PNA)[6] and North Atlantic Oscillation pattern (NAO)[7,8] have been the most prominent teleconnection modes that affect the winter climate in North America[9,10]. The PNA is known to influence precipitation and mountain snowpack in northwestern North America, along with fire weather and wildfire occurrence in central and western North America[11–13]. The NAO marginally affects the mid-latitudes of North America[14–16]. While the impacts of PNA and NAO have been studied broadly, the extent to which these atmospheric teleconnection modes have changed over time has not been adequately examined and attributed. In particular, their relationships with NAWD and their changes in time have not been established.

Dynamically speaking, extreme hydroclimate events in western North America are influenced by stationary waves due to their prolonged influences. Emerging research suggests that mid-latitude climate extremes are

[1]School of Earth Sciences and Environmental Engineering, Gwangju Institute of Science and Technology, Gwangju, Korea. [2]Department of Plants, Soils, and Climate, Utah State University, Logan, UT, USA. [3]School of Earth and Environmental Sciences, Seoul National University, Seoul, Korea. [4]Faculty of Earth and Environmental Sciences, Chonnam National University, Gwangju, Korea. [5]Moon Soul Graduate School of Future Strategy, Korea Advanced Institute of Science and Technology, Daejeon, Korea. e-mail: yjinho@gist.ac.kr

often accompanied by significantly amplified planetary-scale circulation anomalies in the mid-troposphere that determine the spatial structure of teleconnections[17,18]. The amplified stationary wave, partly driven by jet changes, can heighten the likelihood of heat waves in western North America and cold outbreaks in eastern North America[19–21]. However, it remains to be explored how the jet streams, stationary waves, and teleconnection modes (i.e., PNA, NAO, and NAWD) interplay and change in time. It is also uncertain how human-induced climate change influences the atmospheric circulations in mid-latitudes and teleconnection modes around North America in the present and future climate[22–24].

Here, we document robust changes in the patterns and interconnectivity of the PNA and NAWD over the past several decades. The link between NAO and NAWD is subtler, suggesting a fluctuating yet tentative relationship. We then unveil a plausible mechanism responsible for the observed changes that involve the interaction of the Asia-Pacific jet and the topography in western North America. The proposed mechanism hypothesizes that greenhouse gas-induced warming and the associated poleward shift of the Asia-Pacific jet as the origin of the observed interdecadal changes in the atmospheric teleconnection modes.

Results

Changing teleconnection patterns and strengthening winter stationary wave across North America

Over the last seven decades, noticeable shifts have occurred in the spatial patterns of the wintertime (December–January–February) precipitation in the Pacific Northwest and Northern California (Supplementary Fig. 1b, shading) regressed against the PNA, NAO, and NAWD indices (see Methods for calculation of indices). For the period of 1951–1980 (referred to as T1 hereafter), a pronounced negative regression with respect to PNA was observed over the western U.S. However, this pattern reversed into a positive regression in the recent period of 1991–2020 (hereafter T3) via a transition period of 1971–2000 (hereafter T2) (Fig. 1, PNA). Here, we chose 30 years as a standard benchmark for dividing the longer timeframe. The division of the periods into T1, T2, and T3 was conceptualized with specific climatological phases in mind; T1 represents the past climatology, T2 serves as a transition period, and T3 denotes the recent climatology. For the NAO, while positive regression coefficients existed over the Pacific Northwest in the past, they became statistically insignificant even with opposite signs in recent decades (Supplementary Fig. 1b, NAO). On the other hand, the NAWD index exhibits a potent influence on winter precipitation throughout the analyzed period, with a steadfastly negative regression pattern over western North America (Fig. 1, NAWD). Detailed chronological changes can be reviewed in Supplementary Fig. 1b.

The patterns of circulation anomalies associated with the three atmospheric teleconnection modes have undergone systematic variations as well (Supplementary Fig. 2). Regression patterns of the zonal mean-removed 200-hPa geopotential height (eddies) revealed the following. (1) The PNA regression pattern with a negative center over the central Pacific and a positive over North America shifted slightly eastward (Supplementary Fig. 2a). (2) The NAO regression pattern exhibited a significant positive trend over the Alaskan coast (Supplementary Fig. 2c) from T1 to T3. (3) The NAWD regression pattern retained its consistency with a positive center near the Alaskan coast and a negative near northeastern North America, but the magnitude and area of the pattern became larger in T3 (Supplementary Fig. 2b).

In the recent period (T3), a spatial correlation has emerged between the regression patterns of different indices: a negative association between the PNA and the NAWD regression patterns and a weak correspondence with the NAO in relation to recent winter precipitation (Supplementary Fig. 1b, right column). This interconnection has strengthened over the last 70 years, as evidenced by the more pronounced recent regression patterns obtained from the eddy geopotential height (Supplementary Fig. 2, bottom). The evolving interrelationships among the three atmospheric teleconnection modes have been delineated by analyzing the 30-year sliding correlation between each index (Supplementary Fig. 1a). While past correlation coefficients between the PNA and the NAWD and those between the NAO and the NAWD were nearly zero and insignificant, the negative PNA-NAWD has intensified since the late 20th century (Supplementary Fig. 1a green line), coupled with an insignificant or only a marginally significant correlation of NAO–NAWD (Supplementary Fig. 1a, brown line). These time-varying correlation results indicate that the intrinsic variability of each atmospheric teleconnection mode used to operate more independently in the past, but they have been interacting more closely in recent decades, potentially amplifying their (collective) effects. It appears that the NAWD

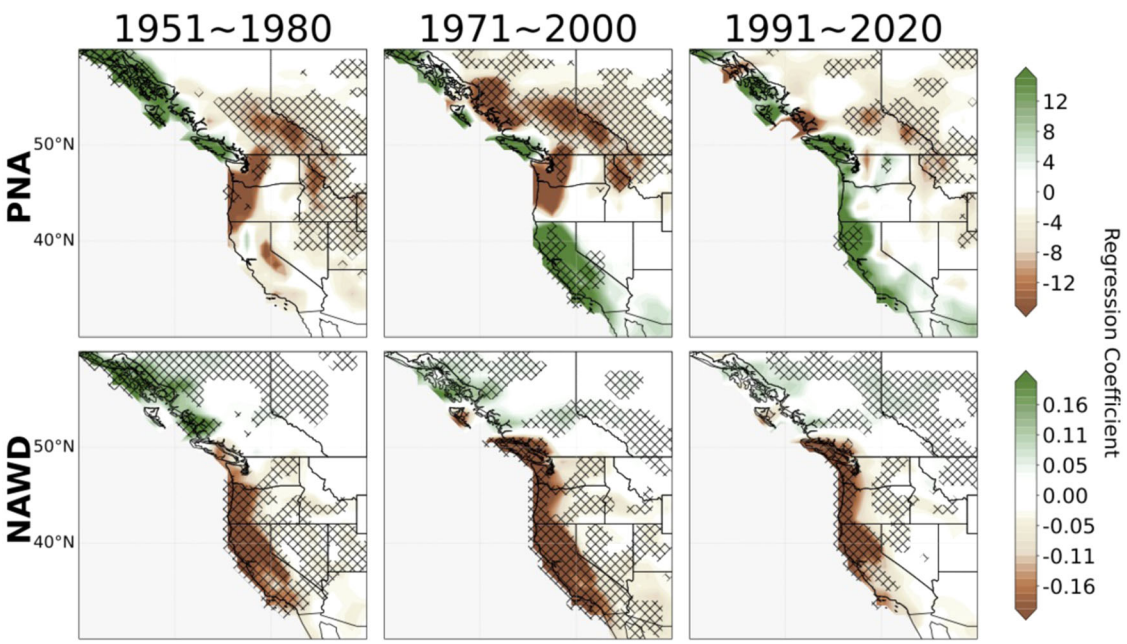

Fig. 1 | The regression map between different atmospheric teleconnection indices (PNA, NAWD) and precipitation during the northern winter season (DJF) for a 30-year period starting from 1951 to 2020. Regression map between different atmospheric indices for PNA (upper), NAWD (lower), and boreal winter (DJF) precipitation during a 30-year period (units: mm per standard deviation). The linear trend is removed in advance. Only significant results are hatched ($P < 0.05$).

teleconnection mode may have been serving as a catalyst linking the PNA with the NAO, a previously unexplored process that is examined herein.

The systematic changes in the patterns of circulation anomalies associated with PNA, NAO, and NAWD could be caused by those in the background flow over North America, which is largely determined by the location and intensity of the stationary waves. To test this idea, we analyze how 30-year averages of 200-hPa eddy geopotential height change during the analysis period. Figure 2a shows the time means of 200-hPa eddy geopotential height for 1951–1980 (T1), 1971–2000 (T2), and 1991–2020 (T3). The most pronounced change from T1 to T3 in western North America is the gradual development of positive eddy geopotential height anomalies to the east of Alaska, which indicates an eastward expansion of the climatological ridge centered around the western coast of Canada. The strengthened climatological anti-cyclonic circulation decreases the stationary Rossby wavenumber[25,26] in the Pacific Northwest by altering the magnitude and meridional shape of the mean wind in that region (Supplementary Figs. 3 and 4).

To investigate how the changes in stationary wave pattern are associated with the interannual variability, we show the standard deviation of eddy geopotential height (shaded) together with the anomalous eddy geopotential height in each period (contour) in Fig. 2b. The interannual variability, to which the teleconnection modes have large contributions, notably weakens in the Pacific Northwest, where the stationary Rossby wavenumber decreases (Supplementary Fig. 4c), while keeping its magnitude to the west and to the east. The changes in the regression patterns of the teleconnection modes (Supplementary Fig. 2, bottom) align with the observed shifts in the high-standard deviation locations to either side of the intensified high-pressure anomaly ridge, hinting at a potential linkage between the changes in teleconnection strength and the shifts of the winter stationary waves. The zonally confined reduction in the stationary Rossby wavenumber would suppress the poleward and eastward propagation of the stationary Rossby waves. With limited paths for stationary Rossby waves, the patterns of different atmospheric teleconnection patterns may be forced to increasingly resemble each other, indicative of the jet's role as waveguides for the propagation of Rossby waves[27].

To gain more insights into the elevated upper-level anomaly over western North America, a 200-hPa eddy geopotential height anomaly index (ZE200 anomaly index) is created by area-weighted averaging around the positive anomaly center point (see "Methods") along with its 30-year running mean (Fig. 2c). The multi-reanalysis datasets reveal that ZE200 anomaly index shows a pronounced linear trend after 1980. To compare this sharp incline of ZE200 with the declining trend of sliding correlation coefficients, the 30-year sliding correlation between the PNA and the NAWD index is recalculated for the extended period (Fig. 2d). In corresponding to the intensified ridge over North America, a pronounced negative trend is observed in the PNA-NAWD correlation, which has not been observed in the past. This result suggests that the recent conspicuous changes in atmospheric teleconnection modes around North America can be largely attributable to stationary wave changes over western North America. The changing NAO connection is omitted due to its lack of significance in the correlations.

Potential cause(s) for the strengthening of winter stationary waves

The stationary waves are typically organized by zonally asymmetric forcings in mid-latitudes. Such forcings include regionally centered diabatic heating, land-sea contrast, and topography[26,28–34]. So, the strengthening of these stationary waves over the last 70 years is likely due to a mix of all these complex things happening together. Our study aims to identify a specific contributing factor that has recently grown in strength and behaves like these stationary waves, as it could offer a viable explanation for the observed changes. We are particularly interested in exploring the possibility that the influence of terrain on the varying background flow (orographic forcing) could be a primary driver of these changes. The large mountains are crucial in generating planetary-scale stationary waves that set the upper-level ridge over western North America[35–40]. In this context, the Alaskan mountain ranges and the related orographic gravity wave drag are of primary interest. Using NCEP R1 data, we calculated the interdecadal variation of surface orographic wave drags and found that the anomalous meridional surface gravity wave drags near the Alaskan coast (60°N, 140°W) has increased from earlier period (T1) to recent period (T3) (Fig. 3a, shading). This is also corroborated by the results obtained from the more modern ERA5 dataset (Supplementary Fig. 6), thereby affirming our findings. Surface gravity waves can trigger upward motion by mountain lifting[41,42], So, it is dynamically possible

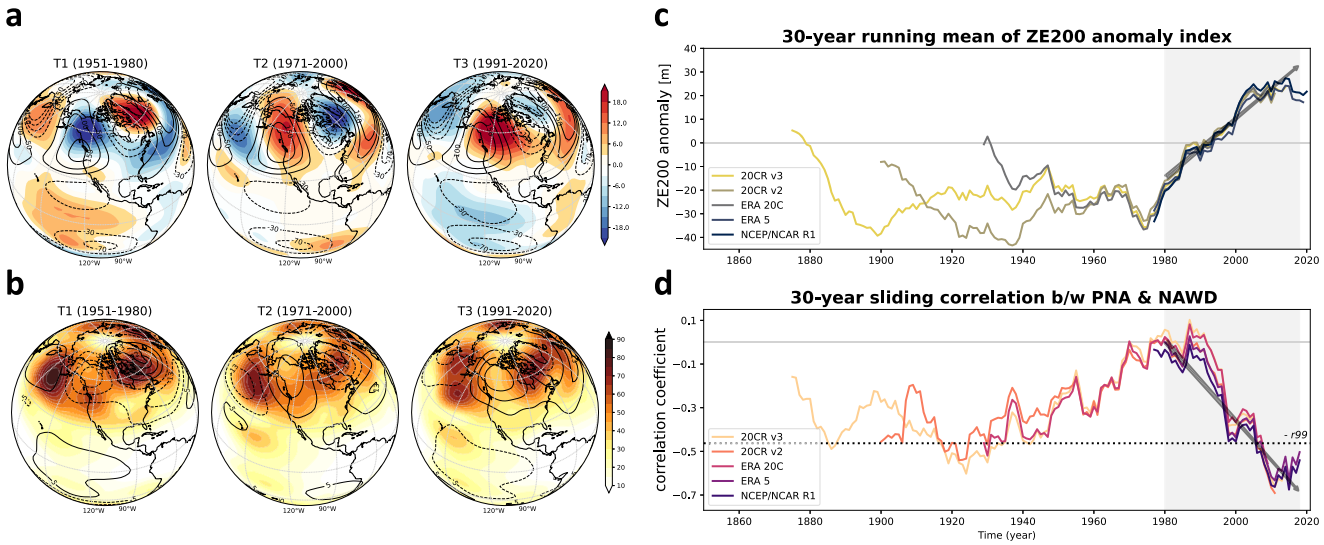

Fig. 2 | Variation of the ZE200 during the northern winter (DJF) season and comparison with the corresponding correlation between PNA and NAWD. a The winter (DJF) mean of ZE200 (units: m) climatology (contour) and anomaly (shading) for a 30-year period starting from 1951 and for T1, T2, and T3. The base period is from 1951 to 2010. **b** As in (**a**), but for standard deviation (shading) and anomaly (units: m), repeated from a, is shown in contour. **c** The time series for the 30-year mean of the ZE200 anomaly index during winter from multi-reanalysis data. The winter (DJF) mean of the ZE200 anomaly index is made by 5° × 5° area average from the high-pressure anomaly center (55°N, 115°W, red line). **d** Recalculate the 30-year sliding correlation from multi-reanalysis data. The Linear trend is removed, and the winter (DJF) mean is applied in advance. The significance at the 99% (black) levels is shown by the dotted line.

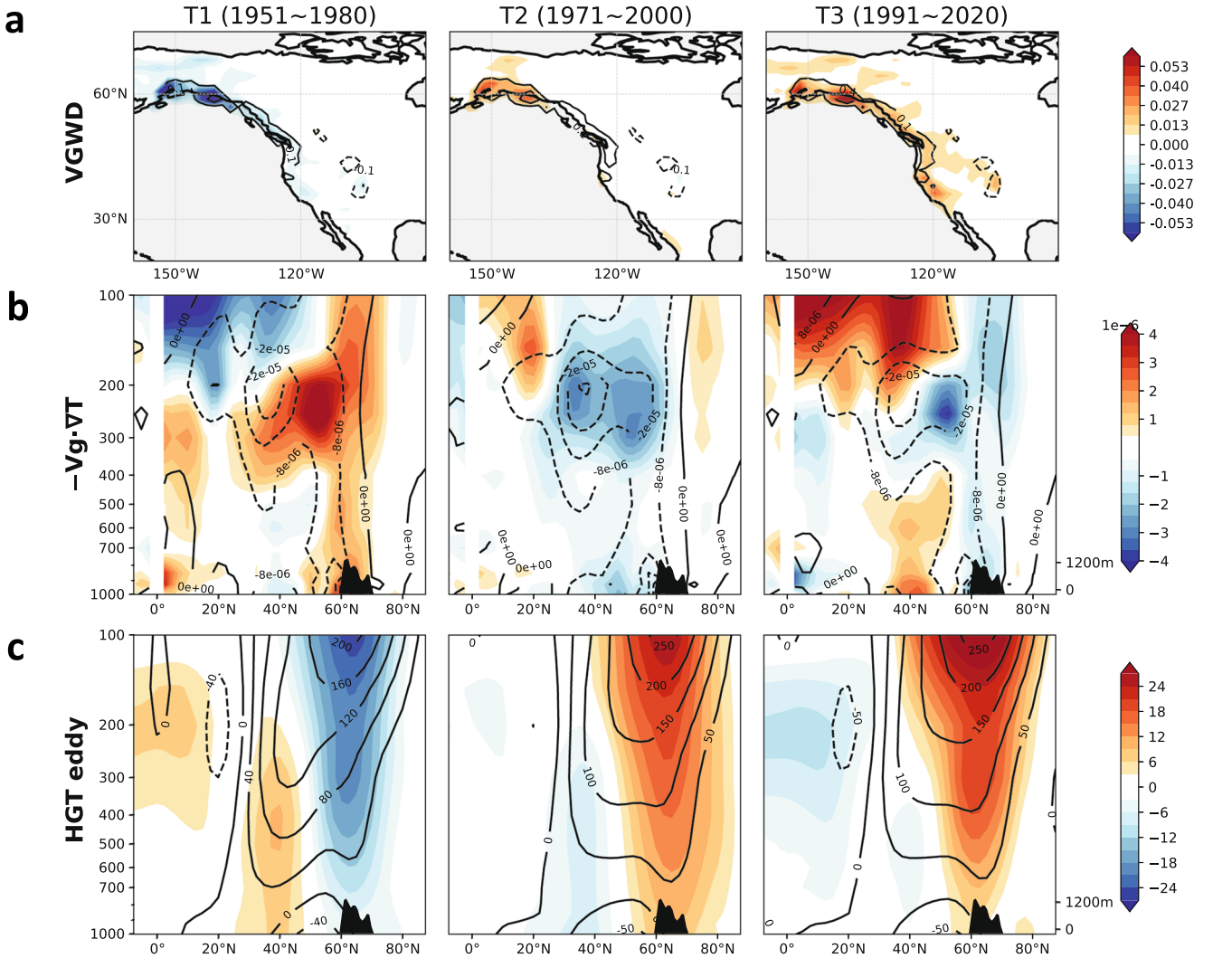

Fig. 3 | Changes in the 30-year mean of the eddy geopotential height vertical structure and temperature advection attributed to meridional surface orographic gravity wave drag (VGWD). a The winter (DJF) mean of meridional surface gravity wave drag (units: Nm^{-2}) climatology (contour) and anomaly (shading). **b** The temperature advection (units: $K\ s^{-1}$) climatology (contour) and anomaly (shading) from the quasi-geostrophic tendency equation. **c** The zonal mean (150–130°W) of winter (DJF) eddy geopotential height (units: m) climatology (contour) and anomaly (shading) for a 30-year period starting from 1951 and for T1, T2, and T3. The topography for the Alaskan range is represented in black color.

that such orographic wave drags near the Alaskan range modulate the upper-level ridge over western North America. This, in turn, contributes to the amplitude changes of winter stationary waves.

The interdecadal variation of upward motion over the strong meridional gravity wave drag, which demonstrated a notable increase near 60°N reaching almost 200-hPa level (Supplementary Fig. 5c, shading), is further analyzed. The detected changes can be accounted for by the temperature advection, with anomalous cold advection in the upper troposphere and warm advection in the lower troposphere in T3, which indicates the increase of geopotential height (Fig. 3b, shading). An additional inspection of the winter Snow Cover Extent (SCE) over the past 54 years reveals a declining trend in the vicinity of the Alaskan coast (Supplementary Fig. 7a), where the reduced snow coincides with the marked increase in warm advection (see Fig. 3b, T3 shading) during the last 30 years (see Supplementary Fig. 7b), indirectly suggesting that circulation changes in the Northeast Pacific might have contributed to the warming and SCE decline. In contrast, a positive anomaly in snow cover extent is seen in northeastern North America, echoing the amplified NAWD with its eastern trough counterpart. As a result of these processes, an increase in the upper-level eddy geopotential height in recent decades (T3) can be achieved (Fig. 3c, shading).

By computing the weighted area-averaged surface meridional gravity wave drag index (VGWD) (see "Methods" for further details), we further examined the spatial coherence of the orographic gravity wave drag. The ZE200 and VGWD anomaly indices reveal a consistent upward trend and increased variability over the last 70 years (Supplementary Fig. 5b). This implies that modifications in surface orographic gravity wave drag are a significant contributor to the intensification of upper-level ridges over western North America. Under this setting, the interdecadal amplification of the North American stationary waves appears to be barotropic, exhibiting analogous wind circulation properties at both upper and lower levels that could potentially impact surface wave drag (Supplementary Figs. 8b, c). This observation could be influenced by an increased flux of meridional wind from the westerly jet exit. The stress exerted indeed intensifies as the near-surface meridional wind, extending from the jet exit, enhance its interaction with the mountain (Supplementary Fig. 9).

Given that the strengthened upper-level anomaly over western North America was fortified by the northern side of the Asia-Pacific jet core (Supplementary Figs. 10a, b), we next examined the zonal average of the jet

core region (120°E–160°E). This analysis (Supplementary Fig. 10g) indicates a progressively higher latitude with a positive anomaly difference between T2 and T1 and an even larger difference between T3 and T1. These outcomes further suggest that the northward shift of the Asia-Pacific jet core has likely influenced the amplification of the upper-level ridge.

It should be noted that the jet shift and potentially corresponding strengthened stationary waves align with increased western tropical convection and warm SST (Supplementary Figs. 10c–e, h). An earlier study[43] suggests that the latitudinal shifts in the jet core axis were credited to intense tropical western Pacific convection, manifesting as a North Pacific Oscillation (NPO)-like atmospheric circulation pattern. Furthermore, an intensified Hadley circulation, induced by the strengthening of western tropical Pacific convection since the 1990s, has been proposed as a possible factor causing a northward shift of the Hadley circulation boundary and the subtropical jet in East Asia[44]. However, alternative perspectives exist that synoptic transient eddy activity could be a primary driving force in the northward shift of the Asia-Pacific jet[45,46]. Complicating matters further, the influence of western tropical Pacific convection activity varies according to the specific reanalysis datasets considered (Supplementary Fig. 10f). Given this diversity of viewpoints and the associated uncertainty, it appears that a consensus on the core drivers of the jet stream is yet to be achieved, underlining the need for further investigation and validation. In any case, our findings propose that the latitudinal shift of the jet could be a fundamental climatological shift that modulates the variability of upper-level atmospheric circulation over time. Also, this shift could play a role in defining the characteristics and interrelationships of atmospheric teleconnection modes, suggesting a compelling direction for future research to unravel these intricate dynamics.

Previous studies highlight the perspective of Pacific heating and its possible role in driving changes in the upper tropospheric stationary waves over North America[47–50]. Thus, we studied the interdecadal changes of diabatic heating[51,52] and the corresponding Rossby wave source[53] in the winter season. During the last century, there has been a concurrent intensification of the 500-hPa tropical Northwestern Pacific diabatic heating from both NCEP R1 and JRA-55 (Supplementary Fig. 11). This intensification aligns with the observed strengthening of upper-troposphere (200-hPa) positive Rossby wave sources in these regions (Supplementary Fig. 12). Therefore, it seems plausible that the enhanced forcing by both the tropical Northwestern Pacific and the extratropical North Pacific partly explain the amplified winter large-scale stationary waves, which supports the mechanisms proposed by earlier studies[20,47,54]. Moreover, this enhanced forcing could also foster the formation of the relationships among the proposed atmospheric teleconnections.

CESM1-LE attribution

To validate the aforementioned results with climate model simulations, we next examined the Community Earth System Model 1 Large Ensemble Community Project (CESM1-LE) experiments[55]. We found that CESM1-LE did produce the co-variability between the ZE200 anomaly index and the northward shift of the Asia-Pacific jet. However, the 30-year running mean of the ZE200 anomaly index in the mean of 40 CESM1-LE members does not align with the NCEP R1 (Supplementary Fig. 13d, black line), which is not surprising because past variability only represents "one outcome" of the ensemble mean. Nonetheless, CESM1-LE does suggest a northward shift of the Asia-Pacific jet in the recent period (T3) based on its climatological zonal wind at 200 hPa. This trend appears to further amplify in future projections (2031–2060; future time, TF) as the climate further warms (Fig. 4a, CESM1-LE and Supplementary Fig. 13a, c), suggesting a likely signal over noises.

We found a statistically significant linear relationship after plotting the relationship between the CESM1-simulated northward jet shift and the increase in 200-hPa geopotential height over western North America across 40 members (Fig. 4b). Based on the NCEP R1 (red cross), the result is characterized as a much stronger geopotential height coexisted with a northward shift of the jet. Even though the CESM1-LE ensemble means only shows a weak amplification of the winter stationary wave, the scatter diagram clearly demonstrates that those members exhibit a distinct correspondence between northward shifts of the Asia-Pacific jet and marked increases in upper-level geopotential height over western North America.

To identify the individual contributions of anthropogenic greenhouse gases (GHG) and aerosol to the interdecadal northward shift of the jet, the climatological spatial pattern and the longitudinal mean of zonal wind at 200 hPa averaged over 120–160°E (U200) are examined for all 40 members along with runs in the CESM1 Single Forcing Large Ensemble Project[56]. The results of GHG forcing (XAER) experiments (see methods) manifest a strong northward intensification of the Asia-Pacific jet and a consistent uptrend in the ZE200 anomaly index. On the other hand, the aerosol forcing (XGHG) experiments produce a more muted response (Fig. 4a, XAER, XGHG and Supplementary Fig. 13a, c, d). The influence of individual anthropogenic forcings is also observed in the formation of southerly winds near the Alaskan coast, a phenomenon noted as part of the process explaining the intensification of geopotential height in the upper troposphere over western North America (Supplementary Fig. 13b). Interestingly, in the XAER forcing experiment, a more robust southerly anomaly develops towards the future time period (TF), in contrast to, the XGHG experiment's weakening tendency of this anomaly.

The intensification of the wintertime zonal mean westerly jet under global warming has been well-documented[57]. The poleward expansion of the Hadley circulation has been suggested as a consequence of the northward migration of eddy-driven jet[44,58,59]. Dynamically, the warming climate leads the mid-latitude zone of baroclinicity to shift northward alongside the eddy momentum flux convergence. This shift, in turn, influences the westerly winds through eddy-mean flow interaction[45,46,60]. A recent study also suggested that the enhanced SST warming in the extratropical North Pacific resulting from global warming also plays a significant role in driving the northward shift of the jet stream[61]. Thus, despite the complex interplay of diverse factors influencing the latitudinal shift of the westerly jet, the poleward shift of the jet under global warming appears to be robust in the literature. This, in turn, supports the hypothesis that GHG forcing contributes to the northward shift of the Asia-Pacific jet core.

To get a clear picture, we employed a joint plot of kernel density estimation to directly compare the distribution of all ensembles for each CESM1 experiment, concentrating on the two phenomena of interest (Fig. 5). From the historical period (T1) to the future (TF), the mean of the distribution for both the northern side of the jet core (see methods) and ZE200 anomaly indices in the XAER experiment shift towards a stronger positive anomaly. Conversely, in the XGHG experiment, they shift toward a negative anomaly. These trends are reflected in the increasing fraction of attributable risk values in XAER experiments (Supplementary Fig. 14), corroborating previous experimental results. In all experiments, the linear relationship between the two indices is maintained, and notably, this relationship becomes more distinct in the XAER experiment as we progress toward the future (TF) compared to the All forcing experiment. This suggests that the anthropogenic GHG forcing contributes to the acceleration of the linear relationship between the ZE200 anomaly and U200 in the future. Another noteworthy result from all CESM1-LE experiments is the expanding variance of both the Asia-Pacific jet core's north side and upper-level geopotential height anomaly over time (Supplementary Fig. 14). Specifically, the F values from the T1 to TF show statistically significant. This is in line with the previously reported increase in the variance of winter stationary waves over North America as per the future climate change scenarios until 2060 (see ref. 5) and the CESM1-projected variance increase[62]. Our study demonstrates not only an increasing variability in stationary wave patterns but also an augmented variability in the latitudinal jet core. These results indicate a potential intensification of mid-latitude unpredicted weather events in the future.

Notably, our findings indicate that the GHG forcing (XAER) appears to influence recent teleconnection changes, but aerosol forcing (XGHG) does not (Supplementary Fig. 15). Although the relationship between the NAWD and the PNA may not be as strong as seen in the reanalysis results, there is still evidence of a decreasing sliding correlation coefficient tendency

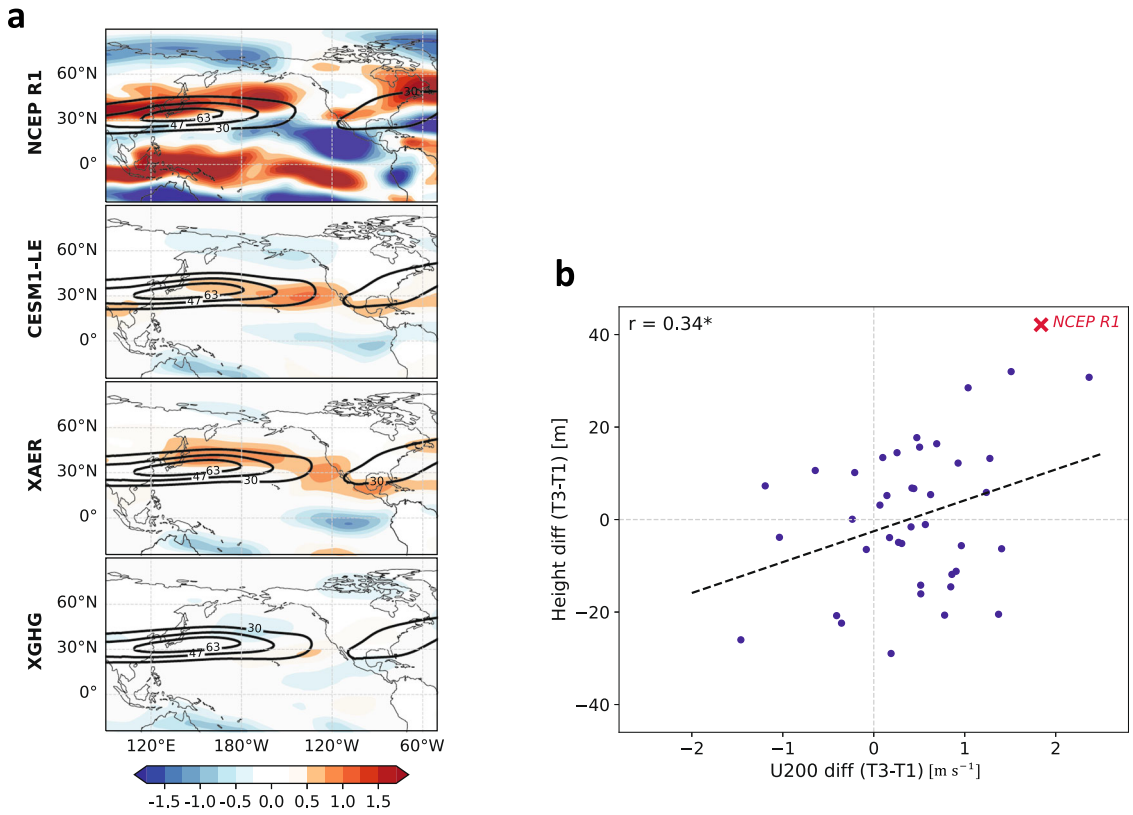

Fig. 4 | Responses of the upper-level (200-hPa) wind to changes in the 30-year mean of ZE200 anomaly index and XAER, XGHG single-forcing run in the CESM1. a The 30-year mean (1991–2020) of U-wind (units: ms^{-1}) climatology (contour) and anomaly (shading) from NCEP-NCAR R1, the mean of CESM1-LE 40 members, XAER (Fixed anthropogenic aerosol forcing in 1920) 20 members, and XGHG (Fixed anthropogenic GHG forcing in 1920) 20 members in boreal winter (DJF). **b** Difference of 200 hPa geopotential height anomaly versus latitudinal jet core difference (northern part of 200 hPa zonal wind anomaly) from the CESM1-LE 40 members (blue mark) with linear regressed line (dotted black). The calculated values from NCEP-NCAR reanalysis 1 are indicated by red crosses. The jet difference was calculated by the weighted area average from the north part of the jet core (30°~45°N, 120°~160°E).The base period for the anomaly is 1951 to 2010. The Correlation coefficient (r) quoted in (**b**) is statistically significant at the 95% confidence level (*).

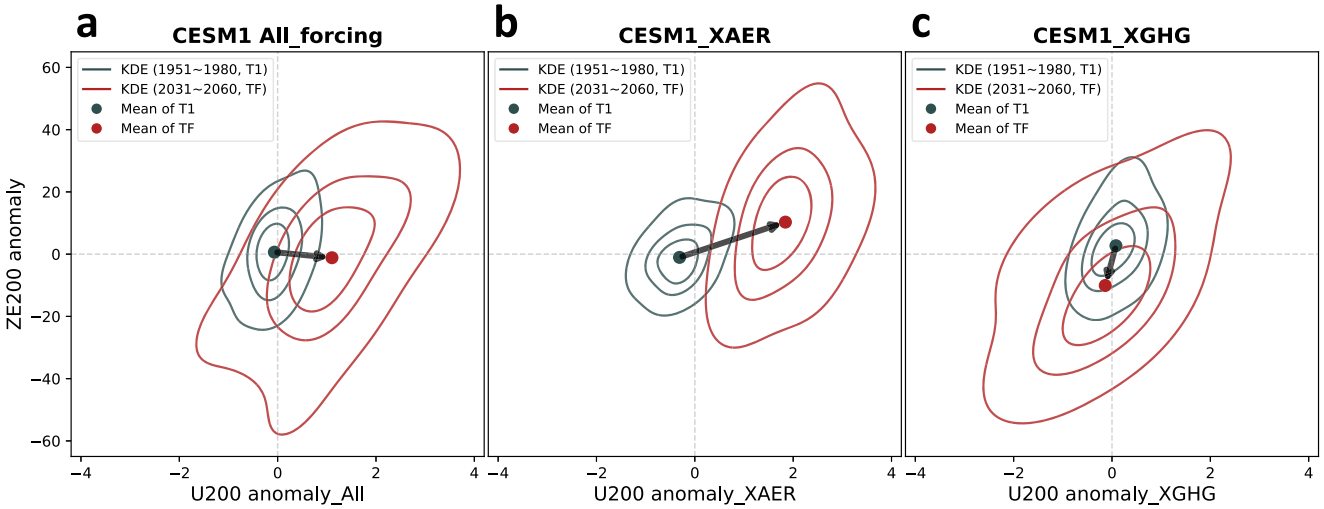

Fig. 5 | Interactions between northward Shift in the 30-year mean of Asia-Pacific jet core and increased upper-level geopotential height over western North America. a–c Joint plot of the northern part of the subtropical jet core (U200) and 200-hPa geopotential height eddy anomaly (ZE200) during the two periods: T1 (blue) and TF (red). The data is derived from CESM1-LE 40 members (**a**), XAER (**b**), and XGHG 20 members (**c**). Two-dimensional Kernel Density Estimation (KDE) is depicted within the box. The mean values of each distribution are represented by blue and red dots, with the change of the mean value indicated by black arrows.

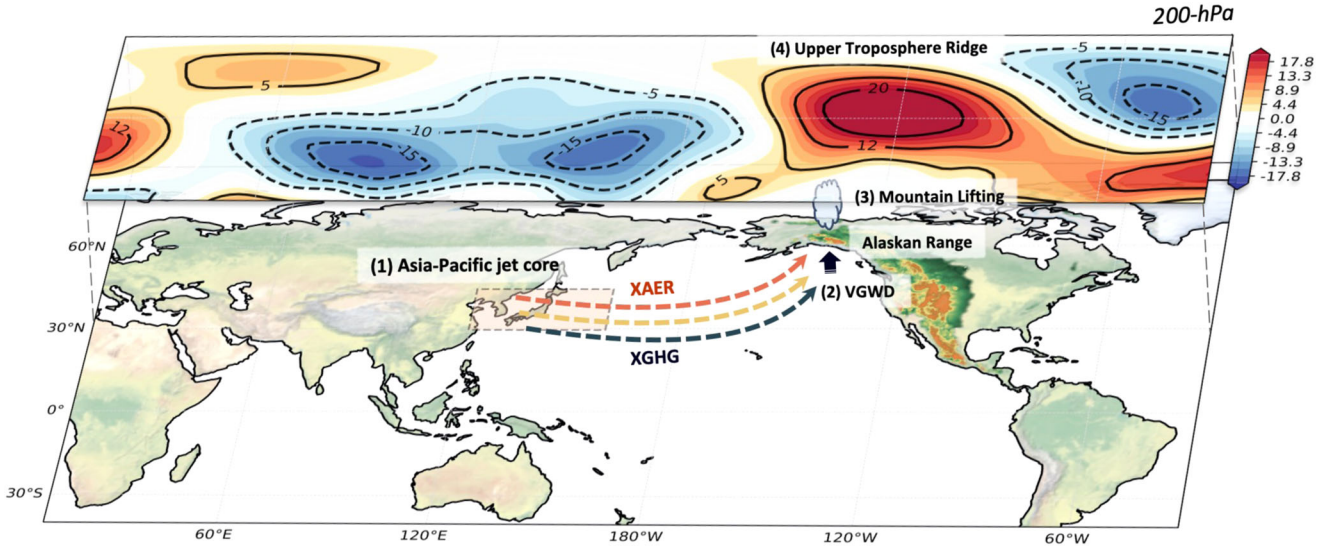

Fig. 6 | Schematic representation illustrating the relationship between the movement of the Asia-Pacific jet core and the increase in upper-level geopotential height. (**1**) Latitudinal motion of the Asia-Pacific jet core according to the CESM1 experiment: XAER(red), XGHG(blue), and CESM1-LE (yellow; All forcing). (**2**) Meridional gravity wave drag (VGWD) caused by southerly winds introduced by the latitudinal movement of the Asia-Pacific jet. (**3**) Mountain lifting as southerly winds reach the Alaskan Range. (**4**) This results in a strengthening of the upper-tropospheric ridge.

in the XAER results, compared to the XGHG. Regardless, GHG forcing is a crucial trigger for the aforementioned changes and should be recognized as an indispensable factor in a future warming climate.

Discussion

In response to the greenhouse gas-induced warming, the Asian-Pacific jet moves poleward, which provokes meridional orographic wave drags to ascend. This lifting resulted in the development of a prominent upper-level ridge over western North America. The ridge alters the paths through which the planetary waves can propagate, affecting the patterns and interconnectivity of the prominent atmospheric teleconnection modes in western North America. The circulation pattern of the PNA has shifted slightly eastward over the central Pacific and North America. Figure 6 summarizes the main findings of our study. The changes in circulation anomaly patterns associated with the PNA led them to have an increasingly negative correlation with the NAWD in recent decades, thus hinting an amplification effect. With a clearer understanding of the relationship between these atmospheric teleconnection modes, the present study elucidates how these patterns evolve together to shape North America's climate variations, which led to a better understanding of future climate extremes and predictability over North America under warmer climate conditions. The complex interplays between these common climate modes cannot be overlooked. Thus, we anticipate that further supporting analyses will unveil the nuanced role of interdecadal variability not only in shaping low-frequency teleconnection modes[63,64] but also in contributing to the variability of large-scale stationary waves and associated mid-latitude storm track dynamics[65–67].

In observations, the NAWD variance has been increasing, leading to more hydrological extremes in California[4]. Moreover, studies have shown stronger variability of the NAWD in climate model simulations with increased GHG concentrations, potentially leading to more severe drought conditions in California[1,68–70]. Our results warrant investigating whether and to what extent the increasing variability of the NAWD affects the variability of the other atmospheric teleconnection modes such as PNA in a warming climate. From a broader perspective, systematic changes in slowly varying large-scale atmospheric circulation have been observed in the past few centuries and are showing apparent signals under human-induced greenhouse gas forcing. These findings provide valuable insights into the intricate interplay among tropics, mid-latitude, and Arctic regions, and can guide future climate modeling endeavors. Certainly, the highlighted significance of Arctic warming and its influence on atmospheric modes is increasingly recognized, suggesting further avenues for research in this realm[66,71–73].

Methods

Observational and CESM1 datasets

We used observed monthly mean of geopotential height, wind (zonal and meridional), omega, air temperature, and surface gravity wave stress (zonal and meridional) data for 1951–2020 from the National Center for Environmental Prediction/National Center for Atmospheric Research Reanalysis Project[74] (NCEP R1), precipitation data from the Global Precipitation Climatology Centre (GPCC)[75], SST data from the National Oceanic and Atmospheric Administration Extended Reconstructed Sea Surface Temperature (NOAA ERSST v5)[76], and Northern Hemisphere Snow Cover Extent (SCE v1) data from NOAA Climate Data Record (CDR)[77]. We further used NOAA-CIRES 20th Century Reanalysis V2[78], NOAA-CIRES-DOE 20th Century Reanalysis V3[79], ECMWF's atmospheric reanalysis of the 20th century (ERA-20C)[80], and ECMWF Reanalysis v5 (ERA5)[81] data to recalculate and compare the consistency of the results for 200-hPa geopotential height eddy anomaly index (ZE200 index) and the 30-year sliding correlation of NAWD and PNA with other data (Fig. 2c, d). The Japanese 55-year Reanalysis (JRA-55)[82] was used to calculate and compare the diabatic heating and Rossby wave source with NCEP R1.

The 40 members of the Community Earth System Model 1 Large Ensemble Community Project (CESM1 LENS) experiments in fully coupled configuration[55] were used for model data with each member constructed using historical climate forcing up to 2005 and subsequent projections based on the RCP8.5 scenario. Also, the 20 members of CESM1 Single Forcing Large Ensemble Project[56] were used to represent individual roles of anthropogenic greenhouse gas (XAER) and aerosol (XGHG) forcing responses. These ensembles employ a model configuration that parallels the CESM1 Large Ensemble Project in terms of the applied forcing configuration and initialization protocol. Notably, conditions related to industrial aerosols (AER) and greenhouse gases (GHG) are maintained at their 1920-year conditions. Simultaneously, all other external anthropogenic and natural forcing factors continue to evolve under the conditions prescribed by the historical and RCP8.5 scenarios.

Atmospheric teleconnection indices (NAWD, PNA, and NAO index)

All indices utilized in this study are based on the mean of winter seasons (December–January-February) from 1950 to 2020. The NAWD index is calculated from the difference between the ridge and trough of the quasi-stationary wave formed in the upper atmosphere of North America during winter. The points for the ridge and trough are determined based on the climatology of the winter average of the 200-hPa geopotential height eddy from the NCEP R1 dataset, spanning the years from 1950 to 2010. After identifying the points of the ridge (48°N, 134°W) and trough (56°N, 80°W), the index is computed through a 5° × 5° weighted area average[1]. In this research, the 200-hPa geopotential height eddy field was used in the calculation of the NAWD index to deal with stationary eddy fields. The Pacific North American (PNA) pattern index, calculated as a single measure reflecting a linear combination of normalized geopotential height anomalies at 500-hPa across four specific centers of action from the Pacific to North America, is obtained using the pointwise method[6]. North Atlantic Oscillation (NAO) index, the surface sea-level pressure difference between the Subtropical (Azores) High and the Subpolar Low, is taken from the National Oceanic and Atmospheric Administration (NOAA) climate prediction center (https://www.cpc.ncep.noaa.gov).

ZE200 anomaly index and VGWD index

The winter (DJF) mean of 200-hPa geopotential height eddy (ZE200) anomaly index is made by 5° × 5° weighted area average from the high-pressure anomaly center ($55^{\circ}N$, $115^{\circ}W$) over western North America. To compare the interannual variability and the long-term trend of ZE200 anomaly index with gravity wave drag, we define a time series is created by conducting a weighted area average of the meridional surface gravity wave drag (VGWD) near the Alaskan range (60°N, 140°W) (Supplementary Fig. 5b).

The northern part of the Asia-Pacific jet core (western North Pacific jet)

Typically, Asia-Pacific jet cores are situated in the 25°-$40^{\circ}N$ latitudinal and the 120–160°E box[43]. To examine the northward shift of the jet, the northern edge of Asia-Pacific jet cores was area-averaged (30–45°N) (Supplementary Fig. 10e).

Fraction of attributable risk for CESM1 output

To compare how the distribution of the 30-year average strength of the north side of the Asia-Pacific jet core and the ZE200 anomaly index changes from the past to the future in each of the CESM1-LE All forcing, XAER, and XGHG single-forcing experiments, we calculate the fraction of attributable risk[83]. It is calculated using the following equation, with the probability of exceedance of the 0.9 quantiles obtained from the past period (T1) condition. This can explain how much the probability of extreme cases for the two phenomena changes.

$$FAR = 1 - \frac{P_{past}}{P_{Future}} \quad (1)$$

Determination of a 30-year period

As per established climatological standards, normal is typically computed over a minimum of 30 consecutive years to capture a meaningful average. This approach is critical in our research, which focuses on interdecadal climatic changes. Analyzing a shorter period could potentially yield trends that diverge from those observed over longer climatic cycles. In addition, the division of the entire study period into T1 (1951–1980), T2 (1971–2000), and T3 (1991–2020) were designed to reflect distinct climatological phases: T1 as the past climatology, T2 as a transition phase, and T3 as the recent climatology. This temporal stratification was intentionally chosen to provide a comprehensive understanding of the evolving climatic trends and patterns, facilitating a more nuanced analysis of the data and its implications.

Data availability

The all meteorological data utilized in this study are freely available for download. The National Center for Environmental Prediction/National Center for Atmospheric Research Reanalysis Project (NCEP R1) data can be accessed at https://psl.noaa.gov/data/gridded/data.ncep.reanalysis.html. The NOAA-CIRES 20th Century Reanalysis V2 is available at https://psl.noaa.gov/data/gridded/data.20thC_ReanV2.html, and the NOAA-CIRES-DOE 20th Century Reanalysis V3 at https://www.psl.noaa.gov/data/gridded/data.20thC_ReanV3.html. The ECMWF's Atmospheric Reanalysis of the 20th Century (ERA-20C) can be found at https://www.ecmwf.int/en/forecasts/dataset/ecmwf-reanalysis-20th-century, and the ECMWF Reanalysis v5 (ERA5) at https://www.ecmwf.int/en/forecasts/dataset/ecmwf-reanalysis-v5. The Global Precipitation Climatology Centre (GPCC) data are available at https://psl.noaa.gov/data/gridded/data.gpcc.html, the National Oceanic and Atmospheric Administration Extended Reconstructed Sea Surface Temperature (NOAA ERSST v5) at https://psl.noaa.gov/data/gridded/data.noaa.ersst.v5.html, and the Snow Cover Extent (SCE v1) data from the NOAA Climate Data Record (CDR) at https://www.ncei.noaa.gov/products/climate-data-records/snow-cover-extent. Additionally, the Japanese 55-year Reanalysis (JRA-55) can be accessed at https://jra.kishou.go.jp/JRA-55/index_en.html. The Community Earth System Model 1 Large Ensemble Community Project (CESM1 LENS) data sets are available at https://www.cesm.ucar.edu/community-projects/lens/data-sets, and the CESM1 Single Forcing Large Ensemble Project at https://www.cesm.ucar.edu/working-groups/climate/simulations/cesm1-single-forcing-le.

Code availability

Analysis for this study was conducted using the NCAR Command Language (NCL) and Python, and the source codes can be made available by the corresponding author upon a justified request.

Received: 27 September 2023; Accepted: 26 February 2024;
Published online: 07 March 2024

References

1. Wang, S. Y., Hipps, L., Gillies, R. R. & Yoon, J. H. Probable causes of the abnormal ridge accompanying the 2013–2014 California drought: ENSO precursor and anthropogenic warming footprint. *Geophys. Res. Lett.* **41**, 3220–3226 (2014).
2. Singh, D. et al. Recent amplification of the North American winter temperature dipole. *J. Geophys. Res. Atmos.* **121**, 9911–9928 (2016).
3. Branstator, G. & Teng, H. Causes of extreme ridges that induce California droughts. *J. Clim.* **30**, 1477–1492 (2017).
4. Wang, S. Y. S., Yoon, J.-H., Becker, E. & Gillies, R. California from drought to deluge. *Nat. Clim. Change* **7**, 465–468 (2017).
5. Wang, S.-Y. S., Huang, W.-R. & Yoon, J.-H. The North American winter 'dipole' and extremes activity: a CMIP5 assessment. *Atmos. Sci. Lett.* **16**, 338–345 (2015).
6. Wallace, J. M. & Gutzler, D. S. Teleconnections in the geopotential height field during the Northern Hemisphere Winter. *Mon. Weather Rev.* **109**, 784–812 (1981).
7. Barnston, A. G. & Livezey, R. E. Classification, seasonality and persistence of low-frequency atmospheric circulation patterns. *Mon. Weather Rev.* **115**, 1083–1126 (1987).
8. Loon, H. V. & Rogers, J. C. The seesaw in winter temperatures between Greenland and Northern Europe. Part I: general description. *Mon. Weather Rev.* **106**, 296–310 (1978).
9. Hartley, S. & Keables, M. J. Synoptic associations of winter climate and snowfall variability in New England, USA, 1950-1992. *Int. J. Climatol.* **18**, 281–298 (1998).
10. Ning, L. & Bradley, R. S. NAO and PNA influences on winter temperature and precipitation over the eastern United States in CMIP5 GCMs. *Clim. Dyn.* **46**, 1257–1276 (2015).

11. Abatzoglou, J. T. Influence of the PNA on declining mountain snowpack in the western United States. *Int. J. Climatol.* **31**, 1135–1142 (2011).
12. Liu, Z. et al. Pacific North American circulation pattern links external forcing and North American hydroclimatic change over the past millennium. *Proc. Natl. Acad. Sci. USA* **114**, 3340–3345 (2017).
13. Justino, F., Bromwich, D. H., Schumacher, V., daSilva, A. & Wang, S.-H. Arctic Oscillation and Pacific-North American pattern dominated-modulation of fire danger and wildfire occurrence. *NPJ Clim. Atmos. Sci*. **5**, 52 (2022).
14. Bai, X., Wang, J., Sellinger, C., Clites, A. & Assel, R. Interannual variability of Great Lakes ice cover and its relationship to NAO and ENSO. *J. Geophys. Res. Oceans* **117**, C03002 (2012).
15. Hurrell, J. W. & Deser, C. North Atlantic climate variability: the role of the North Atlantic Oscillation. *J. Mar. Syst.* **78**, 28–41 (2009).
16. Zhao, H., Higuchi, K., Waller, J., Auld, H. & Mote, T. The impacts of the PNA and NAO on annual maximum snowpack over southern Canada during 1979-2009. *Int. J. Climatol.* **33**, 388–395 (2013).
17. Chen, S. & Wu, R. Interdecadal changes in the relationship between interannual variations of spring North Atlantic SST and Eurasian surface air temperature. *J. Clim.* **30**, 3771–3787 (2017).
18. Wang, L., Liu, Y., Zhang, Y., Chen, W. & Chen, S. Time-varying structure of the wintertime Eurasian pattern: role of the North Atlantic sea surface temperature and atmospheric mean flow. *Clim. Dyn.* **52**, 2467–2479 (2018).
19. Screen, J. A. & Simmonds, I. Amplified mid-latitude planetary waves favour particular regional weather extremes. *Nat. Clim. Change* **4**, 704–709 (2014).
20. Simpson, I. R., Seager, R., Ting, M. & Shaw, T. A. Causes of change in Northern Hemisphere winter meridional winds and regional hydroclimate. *Nat. Clim. Change* **6**, 65–70 (2015).
21. Nakamura, N. & Huang, C. S. Y. Atmospheric blocking as a traffic jam in the jet stream. *Science* **361**, 42–47 (2018).
22. Screen, J. A. & Simmonds, I. Caution needed when linking weather extremes to amplified planetary waves. *Proc. Natl. Acad. Sci. USA* **110**, E2327 (2013).
23. Screen, J. A. & Simmonds, I. Exploring links between Arctic amplification and mid-latitude weather. *Geophys. Res. Lett.* **40**, 959–964 (2013).
24. Wallace, J. M., Held, I. M., Thompson, D. W. J., Trenberth, K. E. & Walsh, J. E. Global warming and winter weather. *Science* **343**, 729–730 (2014).
25. Hoskins, B. J. & Ambrizzi, T. Rossby wave propagation on a realistic longitudinally varying flow. *J. Atmos. Sci.* **4**, 88–100 (1993).
26. Hoskins, B. J. & Karoly, D. J. The steady linear response of a spherical atmosphere to thermal and orographic forcing. *J. Atmos. Sci.* **4**, 88–100 (1981).
27. Teng, H. & Branstator, G. Tropospheric waveguide teleconnections and their seasonality. *J. Atmos. Sci.* **74**, 1513–1532 (2017).
28. Simmons, A. J., Wallace, J. M. & Branstator, G. W. Barotropic wave propagation and instability, and atmospheric teleconnection patterns. *J. Atmos. Sci.* **40**, 1363–1392 (1983).
29. Branstator, G. The relationship between zonal mean flow and quasi-stationary waves in the midtroposphere. *J. Atmos. Sci.* **41**, 2163–2178 (1984).
30. Kang, I.-S. Influence of zonal mean flow change on stationary wave fluctuations. *J. Atmos. Sci.* **47**, 141–147 (1990).
31. Ting, M. & Held, I. M. The stationary wave response to a tropical SST anomaly in an idealized GCM. *J. Atmos. Sci.* **47**, 2546–2566 (1990).
32. Huang, H. H. Relationship between tropical heating and global circulation: interannual variability. *J. Geophys. Res. Atmos.* **99**, 10473–10489 (1994).
33. Polvani, L. M., Esler, J. G. & Plumb, R. A. Time variability and Simmons–Wallace–Branstator instability in a simple nonlinear one-layer model. *J. Atmos. Sci.* **56**, 1445–1460 (1999).
34. Teng, H. & Branstator, G. Connections between heat waves and circumglobal teleconnection patterns in the Northern Hemisphere Summer. *Geophys. Monogr. Ser.* **226**, 177–193 (2017).
35. Chang, E. K. M. Diabatic and orographic forcing of northern winter stationary waves and storm tracks. *J. Clim.* **22**, 670–688 (2009).
36. Garfinkel, C. I., White, I., Gerber, E. P., Jucker, M. & Erez, M. The building blocks of Northern Hemisphere wintertime stationary waves. *J. Clim.* **33**, 5611–5633 (2020).
37. Hartmann, D. L. The atmospheric general circulation and its variability. *J. Meteorol. Soc. Jpn.* **85B**, 123–143 (2007).
38. Sandu, I. et al. Impacts of orography on large-scale atmospheric circulation. *NPJ Clim. Atmos. Sci*. **2**, 10 (2019).
39. White, R. H., Wallace, J. M. & Battisti, D. S. Revisiting the role of mountains in the Northern Hemisphere winter atmospheric circulation. *J. Atmos. Sci.* **78**, 2221–2235 (2021).
40. Held, I. M., Ting, M. & Wang, H. Northern winter stationary waves: theory and modeling. *J. Clim.* **15**, 2125–2144 (2002).
41. Kim, Y.-J., Eckermann, S. D. & Chun, H. Y. An overview of the past, present and future of gravity-wave drag parametrization for numerical climate and weather prediction models. *Atmos. Ocean* **41**, 65–98 (2003).
42. Lott, F. Alleviation of stationary biases in a GCM through a mountain drag parameterization scheme and a simple representation of mountain lift forces. *Mon. Weather Rev.* **127**, 788–801 (1999).
43. Park, J.-H. & An, S.-I. The impact of tropical western Pacific convection on the North Pacific atmospheric circulation during the boreal winter. *Clim. Dyn.* **43**, 2227–2238 (2014).
44. Yeh, S.-W., Song, S.-Y. & Park, J.-H. Change in relationship between the East Asian winter monsoon and the East Asian jet stream during the 1998–99 regime shift. *J. Clim.* **32**, 6163–6175 (2019).
45. Chan, D., Zhang, Y., Wu, Q. & Dai, X. Quantifying the dynamics of the interannual variabilities of the wintertime East Asian Jet Core. *Clim. Dyn.* **54**, 2447–2463 (2020).
46. Zhang, Y. & Stone, P. H. Baroclinic adjustment in an atmosphere–ocean thermally coupled model: the role of the boundary layer processes. *J. Atmos. Sci.* **68**, 2710–2730 (2011).
47. Li, Y., Li, J., Jin, F. F. & Zhao, S. Interhemispheric propagation of stationary Rossby waves in a horizontally nonuniform background flow. *J. Atmos. Sci.* **72**, 3233–3256 (2015).
48. Ma, Q. & Franzke, C. L. E. The role of transient eddies and diabatic heating in the maintenance of European heat waves: a nonlinear quasi-stationary wave perspective. *Clim. Dyn.* **56**, 2983–3002 (2021).
49. Chang, C.-C. et al. An extratropical pathway for the Madden–Julian oscillation's influence on North Atlantic tropical cyclones. *J. Clim.* **36**, 8539–8559 (2023).
50. Chen, Z., Lu, J., Chang, C.-C., Lubis, S. W. & Leung, L. R. Projected increase in summer heat-dome-like stationary waves over Northwestern North America. *NPJ Clim. Atmos. Sci.* **6**, 194 (2023).
51. Zhang, C. & Ling, J. Diabatic heating profiles in recent global reanalyses. *J. Clim.* **26**, 3307–3325 (2013).
52. Zhou, W. & Chan, J. C. L. Intraseasonal oscillations and the South China Sea summer monsoon onset. *Int. J. Climatol.* **25**, 1585–1609 (2005).
53. Sardeshmukh, P. D. & Hoskins, B. J. The generation of global rotational flow by steady idealized tropical divergence. *J. Atmos. Sci.* **45**, 1228–1251 (1988).
54. Tseng, K.-C., Maloney, E. & Barnes, E. The consistency of MJO teleconnection patterns: an explanation using linear Rossby wave theory. *J. Clim.* **32**, 531–548 (2019).
55. Kay, J. E. et al. The Community Earth System Model (CESM) large ensemble project: a community resource for studying climate change in the presence of internal climate variability. *Bull. Am. Meteorol. Soc.* **96**, 1333–1349 (2015).
56. Deser, C. et al. Isolating the evolving contributions of anthropogenic aerosols and greenhouse gases: a new CESM1 large ensemble community resource. *J. Clim.* **33**, 7835–7858 (2020).

57. Polvani, L. & Barnes, E. A. Response of the midlatitude jets, and of their variability, to increased greenhouse gases in the CMIP5 models. *J. Clim.* **26**, 7117–7135 (2013).
58. Lu, J., Chen, G. & Frierson, D. M. W. Response of the zonal mean atmospheric circulation to El Niño versus global warming. *J. Clim.* **21**, 5835–5851 (2008).
59. Lu, J., Vecchi, G. A. & Reichler, T. Expansion of the Hadley cell under global warming. *Geophys. Res. Lett.* **34**, L06805 (2007).
60. Lorenz, D. J. & DeWeaver, E. T. Tropopause height and zonal wind response to global warming in the IPCC scenario integrations. *J. Geophys. Res. Atmos.* **112**, D10119 (2007).
61. Zhou, W., Leung, L. R. & Lu, J. Seasonally and regionally dependent shifts of the atmospheric westerly jets under global warming. *J. Clim.* **35**, 5433–5447 (2022).
62. Stuivenvolt-Allen, J. & Wang, S. S. Data mining climate variability as an indicator of U.S. natural gas. *Front. Big Data* **2**, 20 (2019).
63. Aru, H. et al. Asymmetrical modulation of the relationship between the western Pacific pattern and El Niño–Southern oscillation by the Atlantic Multidecadal oscillation in the boreal winter. *Geophys. Res. Lett.* **50**, e2023GL103356 (2023).
64. Chen, S., Yu, B. & Chen, W. An interdecadal change in the influence of the spring Arctic Oscillation on the subsequent ENSO around the early 1970s. *Clim. Dyn.* **44**, 1109–1126 (2014).
65. Chen, S., Chen, W., Wu, R. & Song, L. Impacts of the Atlantic multidecadal oscillation on the relationship of the spring Arctic oscillation and the following East Asian summer monsoon. *J. Clim.* **33**, 6651–6672 (2020).
66. Chen, S., Wu, R. & Chen, W. Enhanced impact of Arctic sea ice change during boreal autumn on the following spring Arctic oscillation since the mid-1990s. *Clim. Dyn.* **53**, 5607–5621 (2019).
67. Gong, H., Wang, L., Chen, W. & Nath, D. Multidecadal fluctuation of the wintertime Arctic Oscillation pattern and its implication. *J. Clim.* **31**, 5595–5608 (2018).
68. Shi, H. et al. Co-occurrence of California drought and Northeast Pacific marine heatwaves under climate change. *Geophys. Res. Lett*. **48**, e2021GL092765 (2021).
69. Son, R. et al. Recurrent pattern of extreme fire weather in California. *Environ. Res. Lett.* **16**, 094031 (2021).
70. Zamora-Reyes, D., Black, B. & Trouet, V. Enhanced winter, spring, and summer hydroclimate variability across California from 1940 to 2019. *Int. J. Climatol.* **42**, 4940–4952 (2022).
71. L'Heureux, M. L., Kumar, A., Bell, G. D., Halpert, M. S. & Higgins, R. W. Role of the Pacific-North American (PNA) pattern in the 2007 Arctic sea ice decline. *Geophys. Res. Lett.* **35**, L20701 (2008).
72. Liu, Z. et al. Acceleration of western Arctic sea ice loss linked to the Pacific North American pattern. *Nat. Commun.* **12**, 1519 (2021).
73. Tokinaga, H., Xie, S. P. & Mukougawa, H. Early 20th-century Arctic warming intensified by Pacific and Atlantic multidecadal variability. *Proc. Natl. Acad. Sci. USA* **114**, 6227–6232 (2017).
74. Kalnay, E. et al. The NCEP NCAR 40-year reanalysis project. *Bull. Am. Meteorol. Soc.* **77**, 437–472 (1996).
75. Schneider, U. et al. Evaluating the hydrological cycle over land using the newly-corrected precipitation climatology from the Global Precipitation Climatology Centre (GPCC). *Atmosphere* **8**, 52 (2017).
76. Zhang, H.-M. et al. Extended reconstructed sea surface temperature version 4 (ERSST.v4). Part I: upgrades and intercomparisons. *J. Clim.* **28**, 911–930 (2015).
77. Estilow, T. W., Young, A. H. & Robinson, D. A. A long-term Northern Hemisphere snow cover extent data record for climate studies and monitoring. *Earth Syst. Sci. Data* **7**, 137–142 (2015).
78. Compo, G. P. et al. The twentieth century Reanalysis Project. *Q. J. Roy. Meteorol. Soc.* **137**, 1–28 (2011).
79. Slivinski, L. C. et al. Towards a more reliable historical reanalysis: improvements for version 3 of the twentieth century reanalysis system. *Q. J. Roy. Meteorol. Soc.* **145**, 2876–2908 (2019).
80. Poli, P. et al. ERA-20C: an atmospheric reanalysis of the twentieth century. *J. Clim.* **29**, 4083–4097 (2016).
81. Hersbach, H. et al. The ERA5 global reanalysis. *Q. J. Roy. Meteorol. Soc.* **146**, 1999–2049 (2020).
82. Kobayashi, S. et al. The JRA-55 reanalysis: general specifications and basic characteristics. *J. Meteorol. Soc. Jpn.* **93**, 5–48 (2015).
83. Stone, D. A. & Allen, M. R. The end-to-end attribution problem: from emissions to impacts. *Clim. Change* **71**, 303–318 (2005).

Acknowledgements

This research is funded by the National Research Foundation of Korea (NRF-2021R1A2C1011827, NRF-2020M1A5A1110578, and 2021H1D3A2A03097768) and also by Korea Environment Industry & Technology Institute (KEITI) through "Climate Change R&D Project for New Climate Regime.", funded by Korea Ministry of Environment (MOE) (RS-2022-KE002160). S.Y.S.W. acknowledges funding from US NSF P2C2 award number 1903721, the U.S. Department of Energy Award Number DE-686 SC0016605, and SERDP Project RC20-3056. D.K. was supported by New Faculty Startup Fund from Seoul National University.

Author contributions

J.L.: conducted research, created visualizations, analyzed the data, authored the initial draft, and reviewed and edited the manuscript. S.-Y.S.W. developed the study concept, contributed to writing, reviewed and edited the manuscript, and provided oversight. S.-W.S.: developed study concept, contributed to writing, and reviewed and edited manuscript. D.K.: developed study concept, contributed to writing, and reviewed and edited manuscript. J.-H.J.: contributed to writing and reviewed and edited the manuscript. H.K.: contributed to writing and reviewed and edited the manuscript. J.-H.Y.: formulated study concept, conducted research, contributed to writing, reviewed and edited manuscript, and provided oversight.

Competing interests

The authors declare no competing interests.

Additional information

Supplementary information The online version contains supplementary material available at https://doi.org/10.1038/s41612-024-00608-2.

Correspondence and requests for materials should be addressed to Jin-Ho Yoon.